

## Chapter 2

### Technical Aspects: Deposition And Characterization of Photovoltaic Device

#### 2.0 Motivation, Objective, and Abstract

##### Motivation

Patented deposition technology and characterization techniques for laboratory research and commercial industry scale have bench-marked with canon globally. This fosters to look over a deposition technique having less material consumption, fast processing speed, with low cost and maintenance. While the available advanced characterization technique assists with the perception of anatomization.

##### Objective

- To design and fabricate in-situ deposition system for thin film CIGS solar cell module.
- To develop a customized technique for substrate cleaning and annealing process.
- To familiarize with the importance and operational capabilities of characterization techniques befitting the quality and performance.

##### *Abstract*

*The Physical Vapor Deposition (PVD) process offers the feasibility to deposit multilayer thin-films in a vacuum range ( $10^{-5}$ - $10^{-9}$  Torr) even at high temperatures. In current work, the PVD process has circumscribed DC and RF sputtering techniques. In-situ deposition arrangement for multilayer Mo/CIGS/CdS/i-ZnO/AZO have been developed. For the substrate cleaning process, organic followed by plasma cleaning has been deliberated solely. Rapid Thermal Annealing Furnace, which sustains up to 700 °C, has been fabricated for the absorber layer. In-depth investigation of each layer has been carried out with multiple advanced characterization techniques like X-Ray Diffraction, Scanning Electron Microscopy, Atomic Force Microscopy, Raman*

*spectroscopy, Photoluminescence spectroscopy, Elemental Dispersive X-Ray Analysis, X-Ray Florescence, Electrical measurements, UV-Visible-Near Infrared spectroscopy, Current-Voltage measurement, and Spectral Response.*

## **2.1 Deposition Techniques**

In the present work, a thin film of each layer followed by multilayer thin film deposition of the photovoltaic device has been optimized. Thin-film consists of a monolayer of individual atoms or molecules or up to several micrometer (~1 $\mu$ m) thickness. To deposit thin film, deposition techniques are mainly classified as Physical Vapor Deposition (PVD) and Chemical Vapor Deposition (CVD) techniques. Physical vapor deposition is capable of dealing with elements, alloys, and compounds with multilayer deposition thickness of few nanometers to microns range in the vacuum of  $10^{-5}$ - $10^{-9}$  Torr. Vacuum evaporation, Physical sputtering, Arc vapor deposition, and ion plating are classified by PVD techniques. Physical Sputtering occurs when energetic ions bombard the target material and its vaporization in the form of plasma ions on it in a vacuum environment travels from target to substrate without gas-phase collision [1]. In our experiment, we deposited thin film using Direct Current Magnetron Sputtering and Radio Frequency Magnetron Sputtering. In our experiment, both these deposition techniques have been incorporated in vacuum coating (15F6-Hind High Vacuum, Bangalore, India) shown in Fig. 2.1.

### **2.1.1 DC Magnetron Sputtering**

In DC magnetron sputtering, cathode current density depends on the applied voltage. This gives rise to plasma discharge in the abnormal glow region. Here substrate is an anode (grounded) to avoid secondary electron bombardment. In DC sputtering, the cathode attracts ions from the near edge of the plasma region. They impinge on the cathode (target material) with acceleration across the cathode fall region. The impinged ions and energetic neutrals of the sputtering gas cause the ejection of secondary electrons. These electrons move back across the cathode fall region and create ions that are capable of sustaining plasma discharge. Thus, these plasma discharge results in physical sputtering i. e., cathode surface (target material) knock out from its surface. Further, these



**Fig. 2.1: Photograph of Vacuum Coating Unit for multilayer deposition of thin films.**

energetic electrons travel from cathode to anode causing thin film deposition at the anode (substrate). There is a physical collision between energetic ions and neutral species depending upon conditions such as potential, sputtering gas pressure, or vacuum of the deposition chamber.

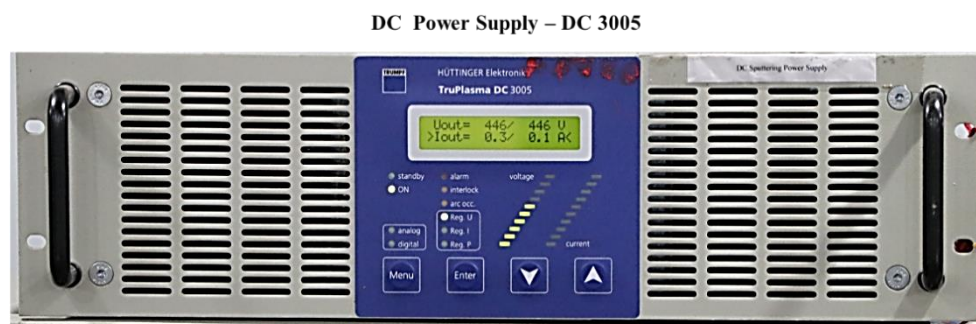


**Fig. 2.2: Photograph of Direct Current (DC) sputtering power supply.**

### **2.1.2 RF Magnetron Sputtering**

Radio Frequency (RF) sputtering itself defines the sputtering technique of where supply is provided to the electrode i. e., applying alternating potential

positive/negative with large peak-to-peak voltage. This voltage is applied to the capacitively charged capacitor. In one half cycle ions are accelerated towards the surface of the target material with an adequate amount of energy due to which sputtering occurs while in another half cycle electrons form a sheath near the surface of the target to avoid charge build-up. The RF discharge can be generated in the 0.5-10 mTorr range and it has an electron density of  $10^9$ - $10^{11}/\text{cm}^3$ . To lessen the loss of actual input power impedance i. e., input power reflects the power supply. Impedance matching network is coupled to the RF electrodes. This impedance matching network reduces the reflected power and allows maximum power to the plasma via the electrode. It is a circuit of low capacitance and low inductance lead. For RF sputtering researchers and commercial industries widely use 0.5-30 MHz range of frequency and mostly widely is used as 13.56 MHz and this technique is applicable for conductive as well as insulating material. If the insulating target material is sputtered by the RF technique, then there will be a low sputtering rate due to some dielectric loss in an insulator target. An insulator target must be backed by the metal conductive target to short out capacitance which is formed due to the metal-insulator-sheath plasma region. In our experiment, we used the RF generator (Model-PFG 600 RF, make TRUMPF Hüttinger Elektronik, Germany) and the impedance matchbox is shown in Fig. 2.3.



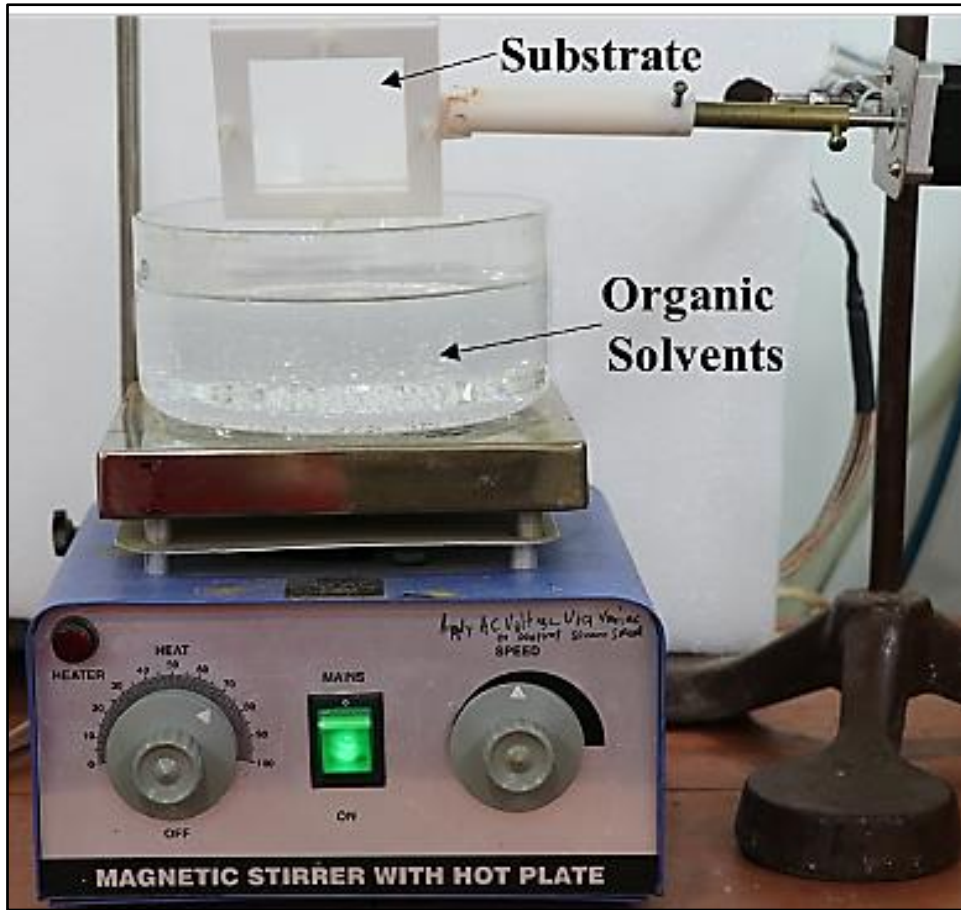
**Fig. 2.3: Photograph of Radio Frequency sputtering power supply and impedance RF Match-Box.**

### 2.1.3 Substrate Cleaning Process

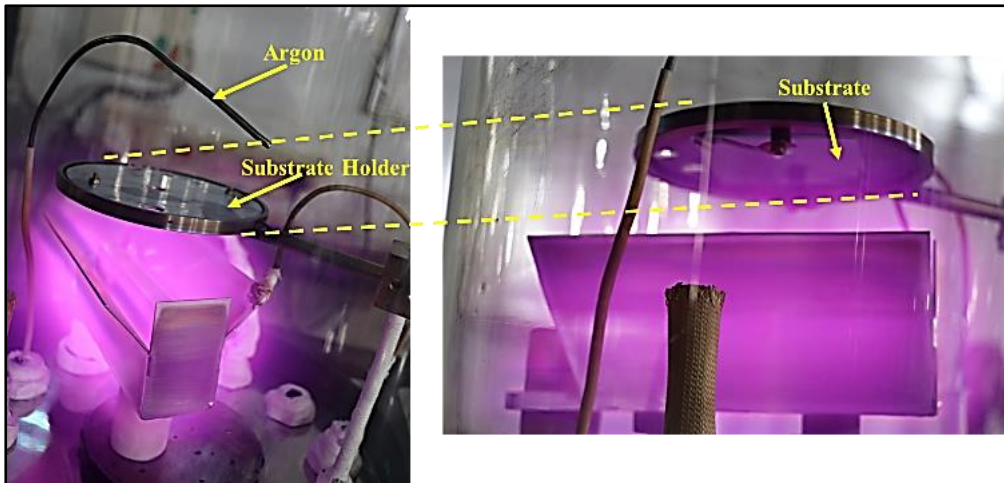
Ultrafine cleaning of substrate is a prime step towards the accomplished thin deposited coatings. In an ambient atmosphere, uncleaned substrate possesses organic, inorganic, dust particles, microbial contaminants. Even during

substrate manufacturing processes, the possibility of raw ingredients, solvents, chemical powder, etc., may present on the surface. Such contaminants are the primary cause of weak adhesion between the substrate surface and deposited layer over it [2]. Wet chemistry is the most widely used process for cleaning which includes, chromic acid, hydrogen peroxide, trichloroethylene, acetone, isopropanol, methanol, and few more such solvents depending on the type and contaminations required to remove. Besides, ultrasonication and heating are provided during the cleaning process. This process has few demerits such as excessive use of chemical solvents, environmental non-friendly due to some extent toxic fumes and allergic to the human body, and residue may remain on the substrate surface due to less purity of the chemical solvent. Plasma cleaning is an inimitable process where high-energy ions are generated with the help of inert gas and voltage supply between anode and cathode. These high energies plasma ions are capable of removing oxides, polar-nonpolar organic and inorganic species, water, and atmospheric dust particles. Plasma ions do not amend the surface properties of the substrate, rather it gently cleans it. This technique is highly adopted by industries and researchers as it provides the ultrafine clean substrate and high adhesion between the substrate surface and layer deposited over it due to high bond strength between them. Apart from this, it has a fast processing speed, uses inert gases, avoids wet chemistry, and eco-friendly.

We adopted a plasma cleaning process for our precleaned 60 x 60 x 1 mm soda-lime glass (SLG) substrate (Marienfeld, Germany). Plasma cleaning in an argon environment was carried out for 20 minutes as shown in Fig. 2.4 (b). Before plasma cleaning, the substrate has stream through the organic cleaning process. During the organic cleaning process initially, the substrate was sprayed with compressed air to remove dust particles. Further, the substrate was rotated as described in Fig. 2.4 (a) over hot (~90 °C) organic solvents trichloroethylene, acetone, and methanol (Fisher scientific AR grade). The vapor of solvents condenses on the surface of the substrate and removes the particles and contaminants on the surface of a substrate.



(a)



(b)

**Fig. 2.4: Soda Lime Glass (SLG) cleaning process (a) Organic cleaning and (b) Plasma cleaning.**

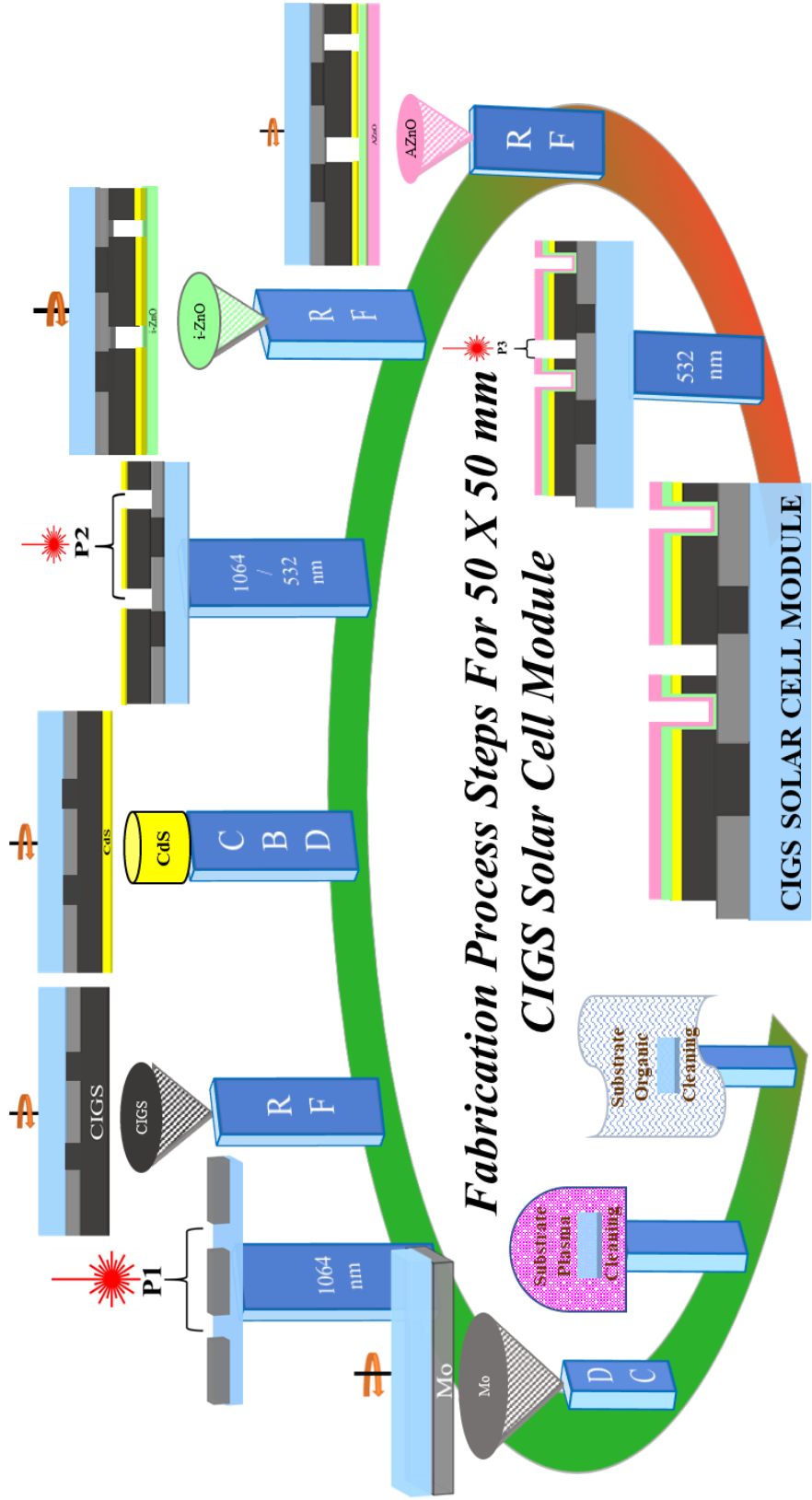
## **2.2 Process Steps Involved: CIGS Solar Cell Module**

We aimed to develop CIGS thin-film solar cell module using one step sputtering process. The fabrication steps include organic followed by plasma cleaning of pre-cleaned 60 x 60 x 1 mm of the SLG substrate. Then sequential deposition of Mo (DC)/CIGS (RF)/CdS (thermal/CBD/RF)/i-ZnO (RF)/AZO (RF) has been carried out in vacuum coating unit in high vacuum environment. CIGS absorber layer has been deposited using one step RF sputtering technique. This technique offers a single composite source rather than individual/multiple deposition sources like in the 2-3 stage of co-evaporation, avoids the toxic H<sub>2</sub>Se gas for selenization, and good composition stability. The balanced magnetron (MAKE: Angstrom Science, USA, and Excel Instruments, Mumbai, India) for sputtering was 2-inches diameter as per the target dimensions. For grain growth of absorber layer, annealing has been carried out in indigenously developed Rapid Thermal Annealing Furnace coupled with temperature profile controller (Selec PR502). The Furnace has the capability of working in a vacuum and an inert gas environment up to a temperature of 700 °C. Monolithic integration P1, P2, and P3 have been made using the Nd:YAG (1064 nm) laser scribing technique. The schematic of the step-wise fabrication process of the CIGS solar cell module is represented in Fig. 2.5 (a). The sputtering target of Mo, CIGS, CdS, i-ZnO, and AZO are installed in a single vacuum coating unit shown in Fig. 2.5 (b) and for the CIGS annealing process, the furnace is shown in Fig. 2.5 (c). The substrate has planetary motion during the deposition for compositional and thickness homogeneity.

## **2.3 Characterizations Techniques**

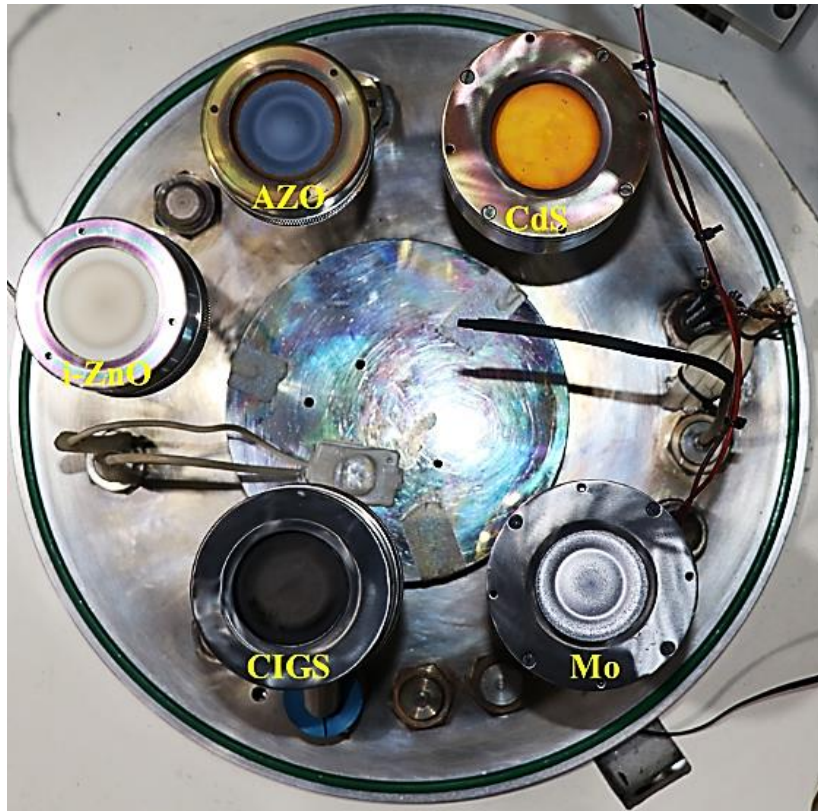
### **2.3.1 X-ray Diffraction**

X-rays are like a wave in nature, when imposed on atoms they get scattered and form constructive interference and collectively form a diffraction pattern. This diffraction pattern possesses crystallographic atomic information of crystals. X-ray diffraction pattern represents the intensity of x-ray of scattered from the

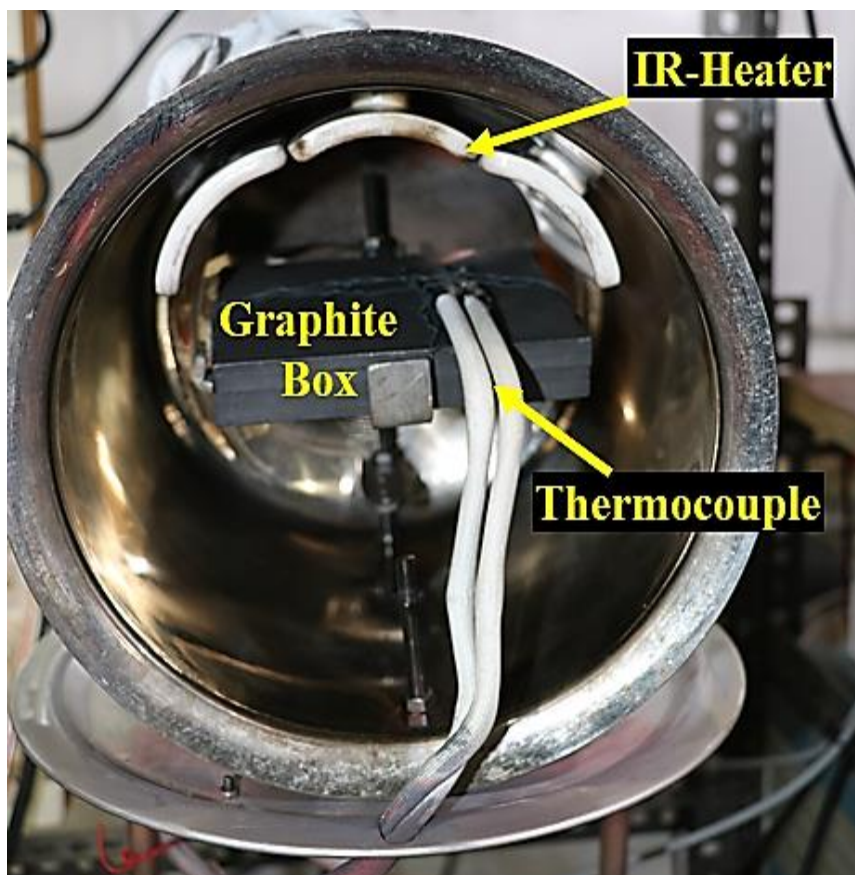


**Fabrication Process Steps For 50 X 50 mm CIGS Solar Cell Module**

(a)



(b)



(c)

**Fig. 2.5: (a) Schematic of Fabrication process of 50 x 50 mm CIGS solar cell module, (b) photograph of sputtering targets used for deposition of Mo/CIGS/CdS/i-ZnO/AZO layers, and (c) Annealing furnace (front view).**

crystal structure at different specific angles. In the graphical depiction, the diffraction position is represented by interatomic distance while the atomic type is the counts of the intensity. Microstructural, defects, and instrument properties contribute to diffraction width and shape. Bragg defined the interrelation between diffraction angle ( $2\theta$ ) and interatomic space ( $d-hkl$ ) where ( $hkl$ ) is the plane normal. He suggested a model for diffraction, where parallel planes of crystal and their interatomic distance defines the peak position. Diffraction angle ( $2\theta$ ) is the angle between the incident x-ray beam and reflected beam receiving at the detector. An incident angle ( $\omega$ ) is half of the detection angle ( $2\theta$ ). A vector that bisects incident and scattered beam at an angle is known as a diffraction vector. When the diffraction vector is normal to the surface of the sample then named as Bragg-Brentano Geometry. This geometry is widely used in X-ray diffraction instruments as shown in Fig. 2.6. A diffractometer is used for the X-ray diffraction study. It consists of integrated components mainly X-ray tube (sealed (1.8-3.0 kW) and rotating (9-18 kW)), monochromators (to remove unwanted radiation from an incident or diffracted beam),  $\beta$ -filters (to reduce the intensity of K-beta and W wavelength radiation) goniometer, incident and receiving beam optics (to reduce the divergence of X-ray beam), parallel beam optics for Bragg-Brentano geometry sample holder and detector (point detectors (scintillation counter, Si) and position-sensitive detector (2D area detector, CCD, Solid-state strips)). X-ray diffraction study is used to analyze phase composition, crystallography, unit cell parameters, Bravais lattice symmetry, residual and micro strain, epitaxy, texture, and crystallite size. Different techniques depending on the sample, parameter, and property analysis X-ray diffraction can be performed through various techniques. They are named X-ray Powder Diffraction, Single Crystal Diffraction, Back-reflection Laue Diffraction, Grazing Incidence Angle Diffraction, X-ray Reflectivity, and Small Angle X-ray Scattering [3].

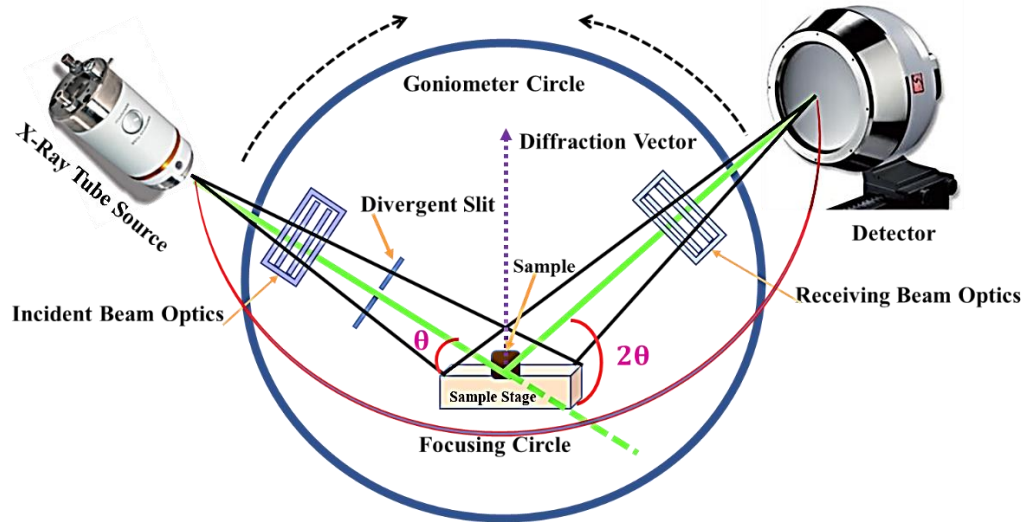


**Fig. 2.6: Schematic diagram of the mechanism of X-Ray Diffraction technique.**

### 2.3.2 Scanning Electron Microscopy

Electrons beam's interaction with ultra-thin specimen results in magnificent, focused images when light microscopy is fizzled out due to its optical and instrumentation features. Scanning Electron Microscopy (SEM) is one of such prominent techniques used to analyze the topography and morphology (size, shape) of the specimen. Fig. 2.7 represents the schematic diagram of the scanning electron microscope [4]. An inelastic collision between specimen and incident electron beam transferring the substantial energy of their primary beam (less than 50 eV) results in the generation of secondary electrons. These secondary electron signals are captured and finally, an image is formed for analysis. SEM instrument is a conglomeration of the electron gun (tungsten filament or field emission gun), electron lens, a condenser lens, objective aperture and electromagnetic scanning coil, signal detector, chamber (specimen stage), and analysis software. Microstructural shape analysis of specimen is highly dependent on electron beam energy and an atomic number of specimens. Electron gun trigger accelerating electrons with energy 0.1-30 keV. Electron guns should be capable of generating stable electrons with high current, smallest possible spot size, adaptable energy, and small energy dispersion. Conventional SEM used tungsten or lanthanum hexaboride ( $\text{LaB}_6$ ) filament operating as thermionic emission by supplying high filament current, both filaments are

heated more than 2800 K to extract an electron from the tip of filament (cathode) and drive them towards specimen (anode). To overcome a few disadvantages of thermionic emission gun such as low brightness, short life-time, and more energy widespread modern SEM use field-emission gun (FEG). In FEG construction, there are two anodes where the first anode is used to extract anode electron when few kilovolts are applied at the tip and the second anode is used to accelerate electrons. There are three types of FEG sources i. e., cold field emission, thermal field emission, and Schottky emitters. Electrons lens de-magnify the electron beam image to form a confined probe on the specimen for high-quality imaging. Highly converged and a collimated parallel stream of the electron beam with the help of condenser lens reach to the anode plate. To convert electron beam into the probe, point i. e. smallest spot size at specimen surface, the objective lens helps to focus and de-magnify the beam. Other than resolution and depth of focus several other parameters such as electron beam energy, lens current, aperture size, working distance, an achromatic and achromatic aberration of the lens also contribute to obtain the smallest possible spot size and beam convergence angle ( $\alpha$ ). It is advisable to operate SEM at lower accelerating for acquiring more surface and topographical details. At high accelerating voltage electrons penetrate more inside the specimen and a high-resolution image is not feasible. The most popular detector used to imagine the specimen is Everhart-Thornley (ET) detector. This detector is capable of supplying (+10 kV) to the scintillator and (+300 V) to the Faraday cage. Finally, the scintillator converts electrons into visible photons which further travel down to the photomultiplier tube. On the display unit, the amplified photons are available. One important thing to be noted that if the sample is non-conductive then coating of (Au, Pt, Au-Pd, and Pt-Pd) of approximately 10 nm thickness should be done to avoid charging at the specimen surface [5].

### **2.3.3 Elemental Dispersive X-Ray Analysis**

Element and its content in the compound can be easily identified using its X-ray characteristics and this technique is known as Elemental Dispersive X-ray Analysis (EDAX). When the incident electron knocks out the electrons from the inner shell of the specimen, the electron transit from a higher energy level to the

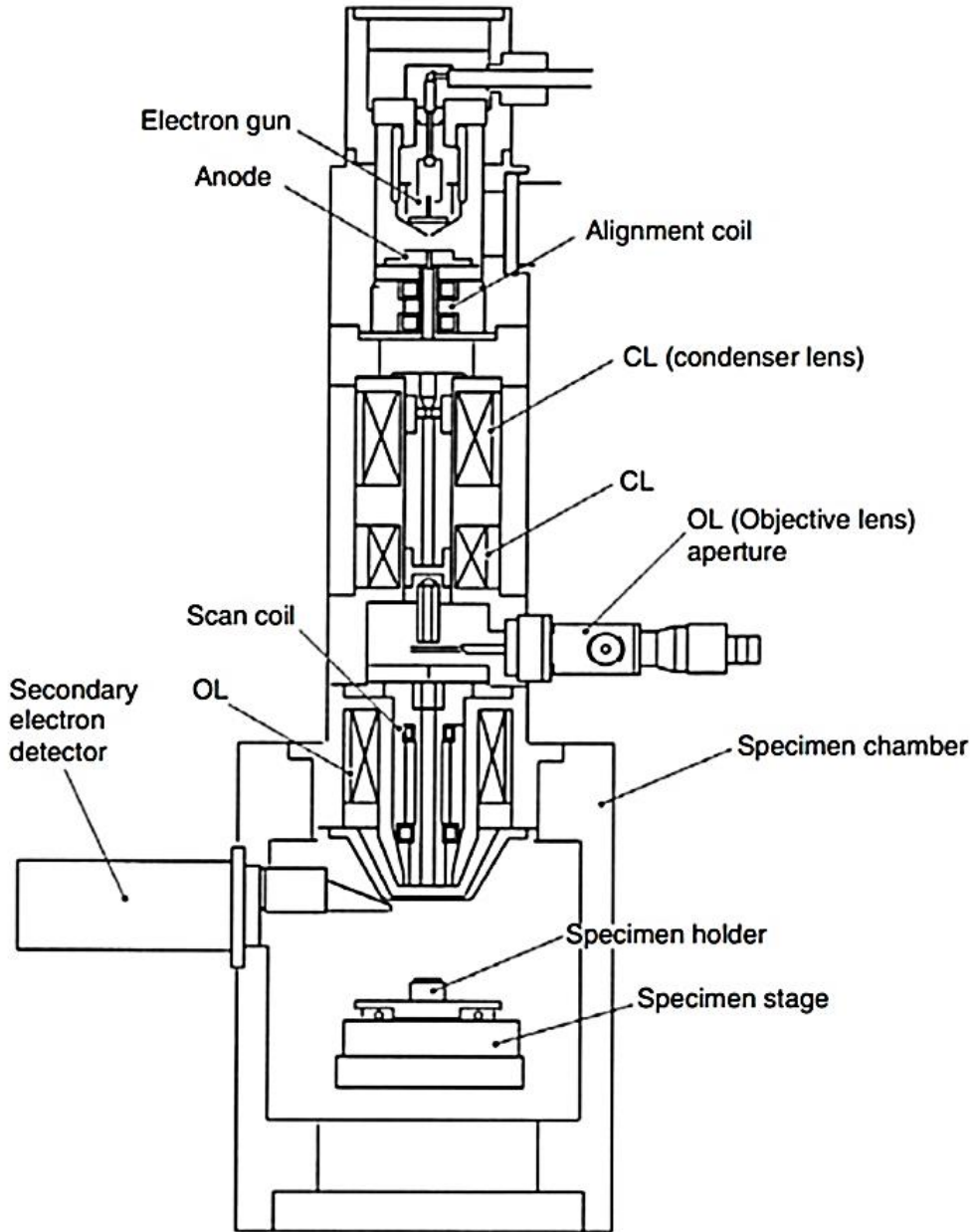


**Fig. 2.7: Schematic diagram of the Scanning Electron Microscope, (JSM-5410, JEOL, USA).**

inner shell level meanwhile it emits an X-ray also. This unique emission of X-ray each element between two energy levels is recorded using a semiconductor solid-state detector (SSD). An element can be identified from its characteristic peak of energy and the integrated intensity of the peak determines the concentration of an element in the specific compound. Generally, SSD is installed within SEM, FESEM, or TEM column. Pure silicon (Si) doped with lithium (Li) is used as SSD where electric charges are proportional to the

amount of energy X-ray produces. The reservoir of charges on the field-effect transistor produces pulse voltage and pulse height [6]. Several pulses commensurable to each pulse height is viewable through a multi-channel pulse analyzer. Elemental spectrum where X-ray energy on the horizontal axis and photon number on the vertical axis is acquired. Element ranging from beryllium (Be) to uranium (U) can be easily determined with an energy resolution of 130-140 eV. EDAX is a non-destructive technique using a small probe current (10 nA), no pretreatment for a sample is required and measurement time is also less.

### **2.3.4 X-Ray Fluorescence**

X-ray Fluorescence (XRF) is an elemental detection technique like EDAX. In XRF, the source is X-rays instead of electrons. It has a similar mechanism of energy transition from a higher level to a lower energy level and the release of excess energy is in the form of an X-ray. Such X-ray is known as 'Fluorescent X-ray' and mechanism is known as 'Fluorescence' [7]. The energy difference between evacuated and replaced electrons is the distinctive characteristic of a specific element. A semiconductor (Si) detector is used for counting and plotting the relative number of X-rays at each energy. As the X-ray interacts with the specimen, the fluorescent X-ray will reach the detector, and electron-hole pair will be generated. The detector will collect the electrons and will result in the current. This current is directly proportional to generated electron-hole pairs which define the energy itself. Depending upon the detector, the detection resolution is ranged 150-300 eV. It can detect elements from sodium (Na) to uranium (U) and concentration from 100 % to ppm-level. It has spot size as low as 10  $\mu\text{m}$  and information depth is higher compared to EDAX.

### **2.3.5 Atomic Force Microscopy**

Atomic Force Microscopy (AFM) reveals the topography of the specimen. It works on the principle of the piezoelectric effect. The cantilever, raster movement, and detector are the prime components of the AFM. The cantilever moves in the X-Y-Z direction over the specimen surface with raster scanning speed. While monitoring the specimen surface, signals (laser beam) is reflected

in the position-sensitive photodetector. This detector captures the lateral and vertical movement of the probe (cantilever) and it plots the 2 D/3D image of the movement of the cantilever in nanometers corresponding to a unit of voltage. The tip of the cantilever is around 5-10 nm in a radius of curvature and have geometry either rectangular or triangular. Cantilevers are made up of silicon or silicon nitride and two important parameters i. e., are spring constant and stiffness of the cantilever dimension defines the image quality. AFM works in three modes: (1) contact-mode, (2) non-contact mode, and (3) tapping mode. The feedback loop is incorporated in tapping mode to control X-Y-Z positions in the AFM stage. Raster scanners are electromagnetic scanner which provides nanoscale motion with highly fast-linear motion. Operation of Atomic Force Microscopy is represented in Fig. 2.8. In contact mode, AFM can be operated in two different modes, one is static force mode in which the probe is in continuous contact with the specimen surface and scans it while another is lateral force mode where scanning is similar to static force mode but in a direction perpendicular to the axis of cantilever. Tapping mode is also known as ‘dynamic mode’ where the cantilever oscillates at a higher frequency or near to resonance. The conventional method of imaging where the amplitude of oscillation is the feedback parameter using tapping mode is ‘amplitude modulation mode (AM-AFM). Other than AM-AFM mode, phase imaging mode where phase contrast or the phase shift of the cantilever oscillation between the drive and response signals is the prime factor to analyze the material properties. Frequency modulation or phase modulation is the feedback parameter. AFM has few advanced imaging mode options like (1) Electric AFM mode (E-AFM) and (2) Magnetic Force Microscopy mode (MFM). A cantilever with the magnetic coating is a probe on the specimen and the magnetic field between tip and specimen is analyzed as phase imaging mode in MFM. E-AFM can be performed in both static and dynamic modes depending upon the required extraction of parameters such as current, surface potential, capacitance, and conductance. In conductive AFM (C-AFM), the current distribution and topography of the specimen are simultaneously mapped. IV curves data can be plotted for a better understanding of the current distribution profile. Piezoelectric Force Microscopy (PFM) responds to the mechanical transformation on the application of an electrical voltage at the cantilever tip.

Electrostatic Force Microscopy (EFM) operates similar to MFM, but here variable electric voltage is applied between specimen and cantilever tip to study the electrostatic effect in the specimen. Kelvin Probe Force Microscopy (KPFM) measures the work function of the specimen by providing contrast imaging through dynamic mode [8].

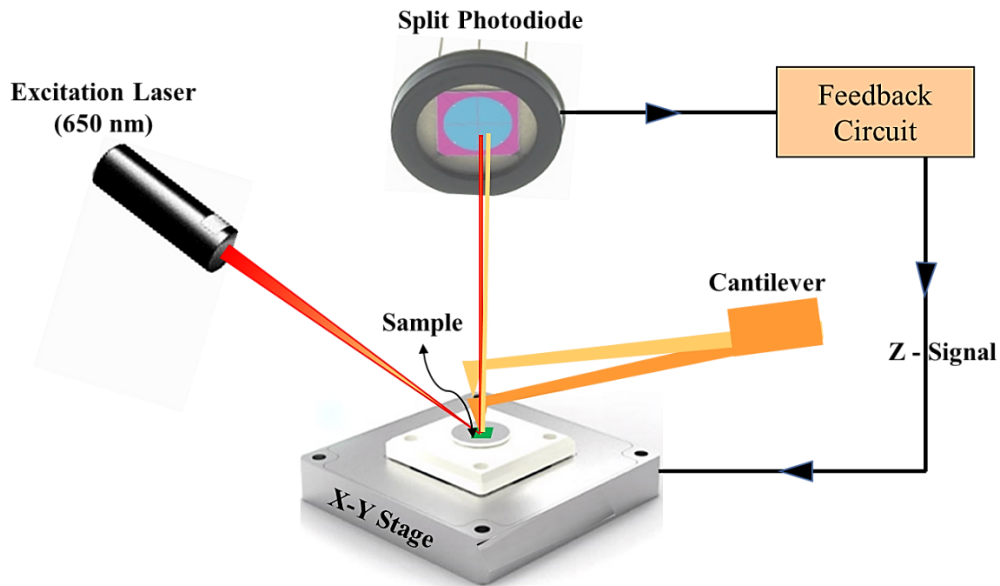


**Fig. 2.8: Schematic diagram of the operation of Atomic Force Microscopy.**

### 2.3.6 Raman Spectroscopy

Properties of semiconductor material like lattice estimation, defects, impurities, free carrier concentration, homogeneity mapping, and surface and interface behavior can be analyzed by the Raman spectroscopy optical technique shown in Fig. 2.9. Raman spectroscopy involves Raman scattering of incoming photons. Non-linear interaction (in-elastically) of incoming photons with carriers, impurities, or phonons transfigure the energy which results in frequency-shift of the outgoing photon. These photons are named ‘Raman scattered photons. They follow the energy-momentum conservation rule where absorbing phonon results in ‘anti-stokes shift’ and losing energy in ‘stoke shift’. Besides, photons are absorbed in infrared wavelength due to the semiconductor optical band feature. Although Raman scattering is a weak process but using a laser as a source satisfies the need the primary need to measure the quality

signal. Raman spectroscopy is a surface analysis as a probe penetrates few nanometers only. To analyze the Raman signal, the setup must be made by considering two major facts: (1) Raman signal is very close to an exciting source (laser) wavelength, and (2) Raman signal is very weak. Raman measurement system has incorporated Fourier spectrometer to indemnify the loss of sensitivity due to intensity scattering. Photomultiplier tube (PMT) and solid-state cooled detectors like InGaAs detectors are capable to cover a broad spectral range with a low signal-to-noise ratio. Polarizable samples are more sensitive to the Raman signal; therefore, it is mostly applicable to understand the orientation of the sample [9].

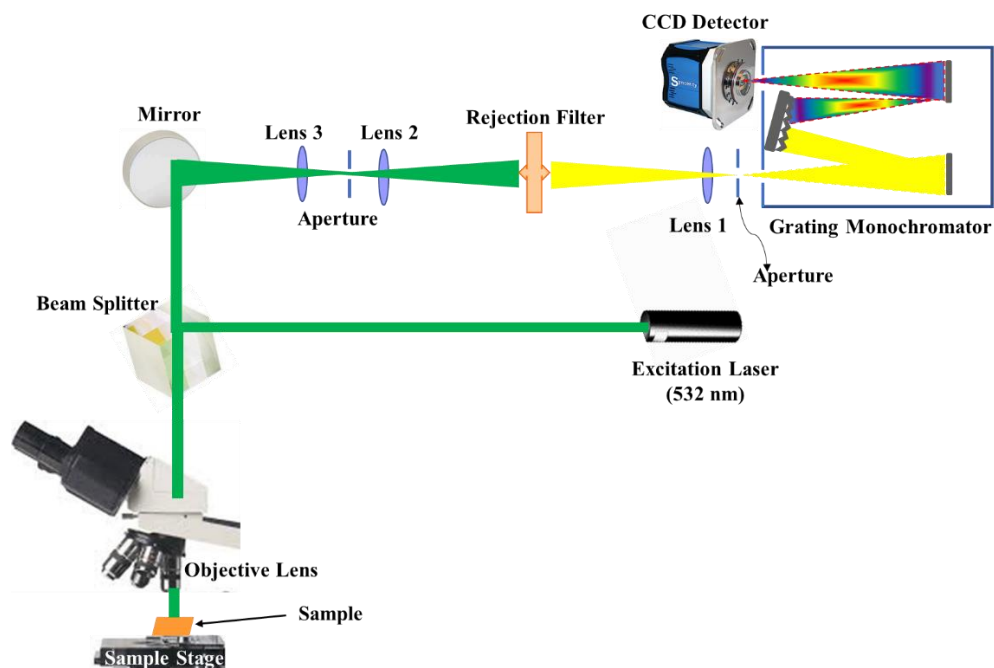


**Fig. 2.9: Optical arrangement for Raman Spectroscopic analysis.**

### 2.3.7 Photoluminescence

Electrons from the valence band to neutral acceptor or a neutral donor to conduction band are capable to induce absorptive transition due to incoming photons. Upon absorbing energy from photons, electrons reach to excited state from their initial state but further, they return to their initial state. While reinstating, electrons experience radiative or non-radiative transitions. In the case of radiative transition, the emission energy spectrum of emitted photons

can be drawn whose energies are the difference between initial and excited-state energy. Two consequences of radiative transitions have been assumed: (1) broad spectral can be obtained when electronic states transitions obey conservation law and (2) non-equilibrium recombination occurs due to the contribution of extra electrons having energies above their equilibrium potentials. In case if the non-radiative process is intense then it can impede the photoluminescence effect. Well, the intermediate state can participate in photoluminescence. Excitons, free carriers including impurities contribute to band-to-band and excitons transitions. Sharpness and finger-print of the emission peak help to understand the bandgap, bandgap offset, compositions, stress, impurity (type and concentration), surface, and interface physical-chemistry. To analyze the photoluminescence of the sample, the excitation source energy should exceed the band-gap of the sample. Continuous laser watts is enough to excite detectable good photoluminescence signals. To reduce the signal to noise ratio, defocusing laser or reducing laser power are adaptable options. The emitted photoluminescence signal from the sample further travels through a monochromator and by selecting a specific wavelength it reaches the detector. The grating of the monochromator defines the spectral range coverage while its focal length measures the resolution and performance capability of the photoluminescence system. PMT, GaAs, Ge, PbS, InAs are special sensitive detectors and provide good results if they are cooled. Using Fourier transformation theory, measurement duration is reduced, and such spectroscopy is known as Fourier transform photoluminescence spectroscopy. To obtain the best spectra, photoluminescence measurement should be carried out at lower temperatures as represented in Fig. 2.10 to avoid thermal broadening of excited charge carriers. It also helps the excited charge carrier to circumvent non-radiative transitions and recombinations [10].

### **2.3.8 Hall Effect measurements**

Electrons in a metallic, semiconductor can be scattered by various mediums such as impurities lattice defects, lattice vibrations, grain boundaries, etc., and this scattering process increases the resistivity of the sample. Two resistivity measuring techniques are widely adopted, one Four Point method for specific finite geometry and with small spacing between the probes, the other method is

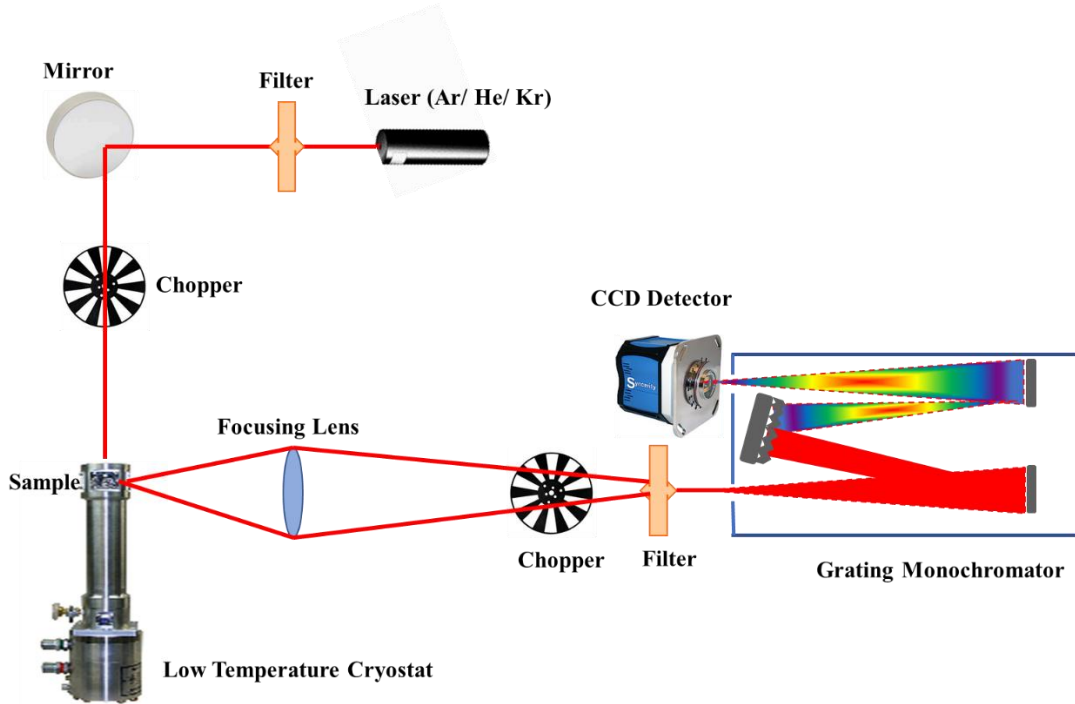


**Fig. 2.10: Optical instrumentation of Photoluminescence spectroscopy with low-temperature arrangements.**

Van der Pauw method where sample geometry is not definite, and probes are space apart placed at the four corners of the sample [11]. In both methods, the contact resistance between probe and sample, spreading resistance due to each probe, and resistance of probe errors can be avoided. Each probe area must be smaller compare to that of the sample. Using the Four-point probe method sheet resistance ( $R_{sh}$ ) can be calculated using the following equation (2.1),

$$R_{sh} = K \frac{V}{I} \quad (2.1)$$

K is the correction factor dependent on the probe to the sample area and sample thickness to probe separation. Van der Pauw's method measures voltages in eight different ways as mentioned below when current I (amp) is a probe in positive dc. Applied DC  $I_{dc}$  should be limited by resistance R of the two probes  $I_{dc} < (200R)^{-0.5}$ .

$$R_{21,34} = \frac{V_{34}}{I_{21}}, R_{12,43} = \frac{V_{43}}{I_{12}}; R_{32,41} = \frac{V_{41}}{I_{32}}, R_{23,14} = \frac{V_{14}}{I_{23}}$$

$$R_{43,12} = \frac{V_{12}}{I_{43}}, R_{34,21} = \frac{V_{21}}{I_{34}}; R_{14,23} = \frac{V_{23}}{I_{14}}, R_{41,32} = \frac{V_{32}}{I_{41}}$$

$R_A = (R_{21,34} + R_{12,43} + R_{43,12} + R_{34,21})/4$  and  $R_B = (R_{32,41} + R_{23,14} + R_{14,23} + R_{41,32})/4$   
 $R_A$  and  $R_B$  are two characteristic resistance related to the terminal, probe, and sample which define sheet resistance  $R_S$  and bulk resistivity  $\rho$  through the van der Pauw equation (2.2) and (2.3);

$$\exp(-\pi R_A/R_S) + \exp(-\pi R_B/R_S) = 1 \quad (2.2)$$

$$\rho = R_S \times d \text{ (thickness of sample)} \quad (2.3)$$

Hall effect is linked with resistivity, voltage is measurable on the current-carrying sample in presence of magnetic field due to Lorentz force driving the charge carriers. Charge carriers travel in a direction perpendicular to the magnetic field and due to internal electric force, they experience Lorentz force in both positive and negative directions of their motion. There will be a potential drop (voltage) across the sample. Such voltage is known as ‘Hall Voltage’. Hall effect follows the ‘right-hand thumb’ rule and further conductivity type, carrier density, and mobility can be derived. To measure Hall mobility, follow the following procedure. Initially apply a constant and uniform positive magnetic field  $B$  in Gauss (G), apply current ( $I_{dc}$ ) an ampere (A) between two leads like  $I_{13}, I_{31}, I_{42}$ , and  $I_{24}$ , and measure  $V_{24P}, V_{42P}, V_{13P}$ , and  $V_{31P}$  between other two leads. Similarly, apply negative magnetic voltage  $B$  and measure the same. Now calculate the offset voltages and be cautious about the magnitude sign of the voltage.

$$V_C = V_{24P} - V_{24N}, V_D = V_{42P} - V_{42N}, V_E = V_{13P} - V_{13N}, \text{ and } V_F = V_{31P} - V_{31N}.$$

Summing voltages  $V_C + V_D + V_E + V_F$  polarity will define the type of material. If it is positive, then (p-type) and negative then (n-type) material. Sheet carrier density ( $\text{cm}^{-2}$ ) can be calculated as per the following equations (2.4) and (2.5).

$$\text{For p-type, } p_s = 8 \times 10^{-8} IB / [q (V_C + V_D + V_E + V_F)] \text{ and} \quad (2.4)$$

$$\text{For n-type, } n_s = |8 \times 10^{-8} IB / [q (V_C + V_D + V_E + V_F)]| \quad (2.5)$$

Where ‘ $q$ ’ is the ( $1.602 \times 10^{-19}$  C) is the elementary charge.

Also, bulk carrier density ( $\text{cm}^{-3}$ ) can be calculated as per equation (2.6) for a known thickness ( $d$ ) of the sample,

$$p = p_s/d \text{ and } n = n_s/d \quad (2.6)$$

From the sheet carrier density  $n_s$  (or  $p_s$ ) and the sheet resistance  $R_S$ , Hall mobility ( $\text{cm}^2\text{V}^{-1}\text{s}^{-1}$ ) is calculated using the following equation:

$$\mu = 1/qn_s R_s \quad (2.7)$$

The measurement techniques i. e., Vander Pauw and Hall Voltage are graphically represented in Fig. 2.11.

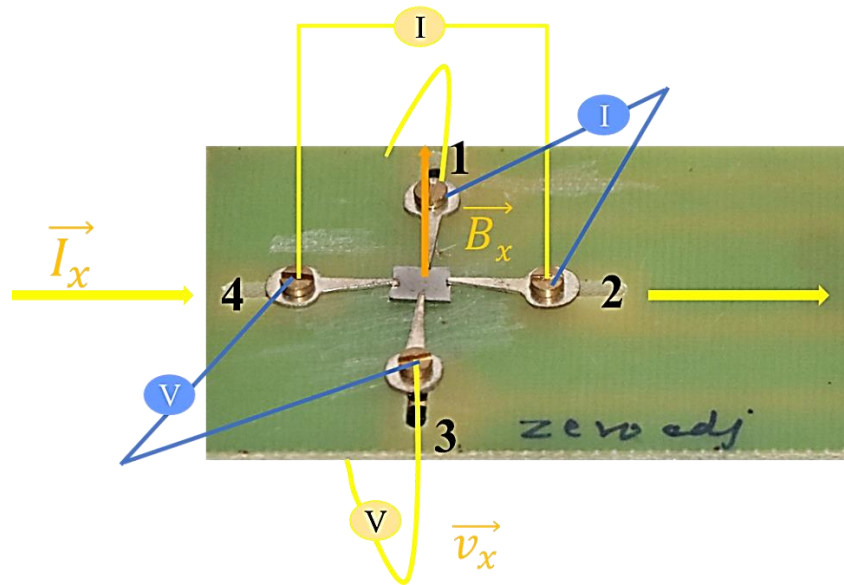
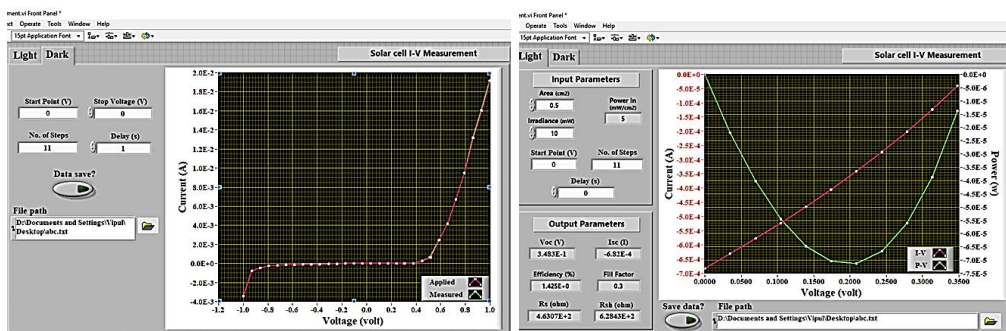


**Fig. 2.11:** Graphical representation of resistivity measurement-Vander Pauw (no  $\vec{B}_x$ ) method (blue color) and Hall-Voltage measurement (yellow color).

### 2.3.9 Current-Voltage (I-V) and Spectral Response

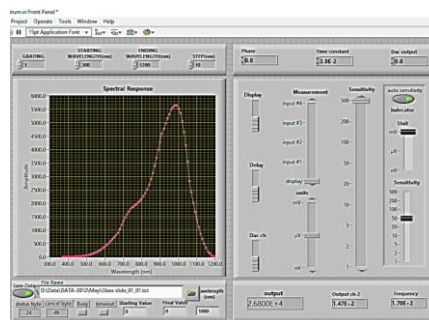
Solar cell performance is evaluated by measuring current-voltage characteristics. Illumination and dark I-V characteristic of the solar cell are noteworthy in extracting parameters like  $V_{oc}$ ,  $I_{sc}$ , FF,  $\eta$  %,  $R_s$ , and  $R_{sh}$ . Under illumination conditions, there is slight instability in photon density which adds substantial noise, and it is difficult to analyze the correct performance of the solar cell. To avoid such issues, dark I-V measurements are analyzed with injected carriers in the device rather than optically generated carriers. Dark I-V measurement gives elementary parameters without using a sun-simulator. series resistance, shunt resistance, diode saturation currents, and diode factor are sensitive to dark I-V measurement. These parameters are efficient to estimate the quality of the junction, the grid, and contact resistances [12]. Under illumination I-V measurement, short circuit current, open-circuit voltage, fill factor, and efficiency are measured. For analyzing dark and illuminated I-V

characteristics of the solar cell, we used illumination sources as metal-halide lamp 150 W. Source meter Keithley 2420 C and digital 6<sup>1/2</sup> 2000 multimeter was used for applying bias voltage and current measurement using four-wire configurations. Automation of I-V measurement was developed with LabView (Laboratory Virtual Instrument Engineering Workbench) 2017. Controlled LabView automation curtails the human errors, measurement time, and direct exposure of metal-halide irradiations. Following Fig. 2.12 (a) and Fig. 2.12 (b) represent the dark and illuminated (Light) I-V LabView automated dialog box. Parameters like start voltage, stop voltage, source delay, source steps can be set and according to them, the source meter will source the current, and the multimeter will measure the voltage. Finally, a dark I-V plot is displayed on the monitor and data can be saved in .txt format. Similar to illuminated I-V measurement, area of the solar cell, input power, and AM 1.5 or AM 1 data can be feed into the program, and illuminated I-V can be obtained.



(a)

(b)



(c)

**Fig. 2.12: Pictorial representation of (a) Dark I-V, (b) Light I-V, and (c) Spectral Response measurement.**

The spectral response of the solar cell is the ratio of the photo-generated current to the incident power on it. Below the bandgap energy, the semiconductor is

ineptitude in absorbing photons of longer wavelength. Above the bandgap energy, solar cells undergo heating as it could not be able to utilize photons having a short wavelength. This signifies the relation between the bandgap and the performance or spectral response of the solar cell. One can estimate the power loss of solar cells based on spectral response. Depending upon spectral responsivity, quantum efficiency can be calculated by measuring the ratio of the output number of electrons from the solar cell to the number of incident photons [13]. Spectral response and quantum efficiency have been measured by the LabView automation program using the following setup shown in Fig. 2.12 (c). Photodetector records the current production by a solar cell, and it converts recorded current into beam power. Using spectral responsivity of the solar cell (device under test-DUT( $I_{DUT}$ ) and responsivity standard photodiode ( $R_{STD}$ ), quantum efficiency (QE) is calculated.

### **2.3.10 Ultraviolet-Visible-Near Infrared Spectroscopy**

Interaction of electromagnetic waves (light beam) with the material will result basically in three phenomena, transmission, reflection, and absorption. Depending on the material's inherent optical properties, it will respond to Ultraviolet-Visible-Near Infrared Spectroscopy. In a transmission incident, the light beam will propagate through the front and back surface of the sample, and in reflection, the incident light beam will reflect from the back surface of the sample. Only non-transmitted and non-reflected light will be absorbed by the sample. Absorption occurs only when the transition frequencies of atoms resonant with the frequency of incident light. The reflection coefficient and the transmission coefficient is termed as 'reflectivity and transmissivity'. The ratio of reflected power to the incident power is known as reflectivity (R) and transmitted power to the incident power as transmissivity (T) [14]. According to the law of conservation of energy as per equation (2.8), in the case of zero absorption or scattering,

$$T + R = 1 \quad (2.8)$$

In the case of optical absorption, the light propagates with intensity 'I' through a medium or sample of thickness 'd' in direction 'z', then attenuation in the

intensity of light is measured in terms of ‘absorption coefficient ( $\alpha$ ). It is expressed in the form of equation (2.9) mentioned below:

$$dI = -\alpha dz \times I(z) \quad (2.9)$$

Further integration of the above equation results into equation (2.10) ‘Beer-Lambert Law’

$$I(z) = I_0 e^{-\alpha z} \quad (2.10)$$

Absorbance can be calculated based on transmission and reflection measurement using the following equation (2.11):

$$T = (1-R)^2 e^{-\alpha d} \quad (2.11)$$

$R=R_1=R_2$ , where  $R_1$  is the reflection from the front surface and  $R_2$  is the reflection from the back surface. The absorption coefficient can be calculated using the following equation:

$$\alpha = \frac{-1}{d} \ln \left( \frac{T}{[1-R]^2} \right) \quad (2.12)$$

Plotting  $(\alpha h\nu)^2$  versus energy ( $E_g$ ) as per equation (2.13) will be able to measure the bandgap energy of the sample.

$$\alpha h\nu \propto (h\nu - E_g)^{\frac{1}{2}} \quad (2.13)$$

We have an in-house setup of UV-Vis-Near IR spectroscopy shown in Fig. 2.13. The setup consists of a Tungsten halogen lamp for visible and near-infrared wavelength region and deuterium arc lamp for UV wavelength region, monochromator (CM110), optical chopper (SR540) with controller unit, beam splitter, Lock-in amplifier (SR530), optical lenses, detectors (Si and Ge), and LabView automated program for data acquisition in computer.

## References

- [1] Donald M. Mattox, *Handbook of Physical Vapour Deposition (PVD) Processing Coatings (Second Edition)*, William Andrew Publishing, Elsevier (2010).
- [2] Peter M. Martin, *Handbook of Deposition Technologies for Films and Coatings (Third Edition)*, William Andrew Publishing, Elsevier (2010).

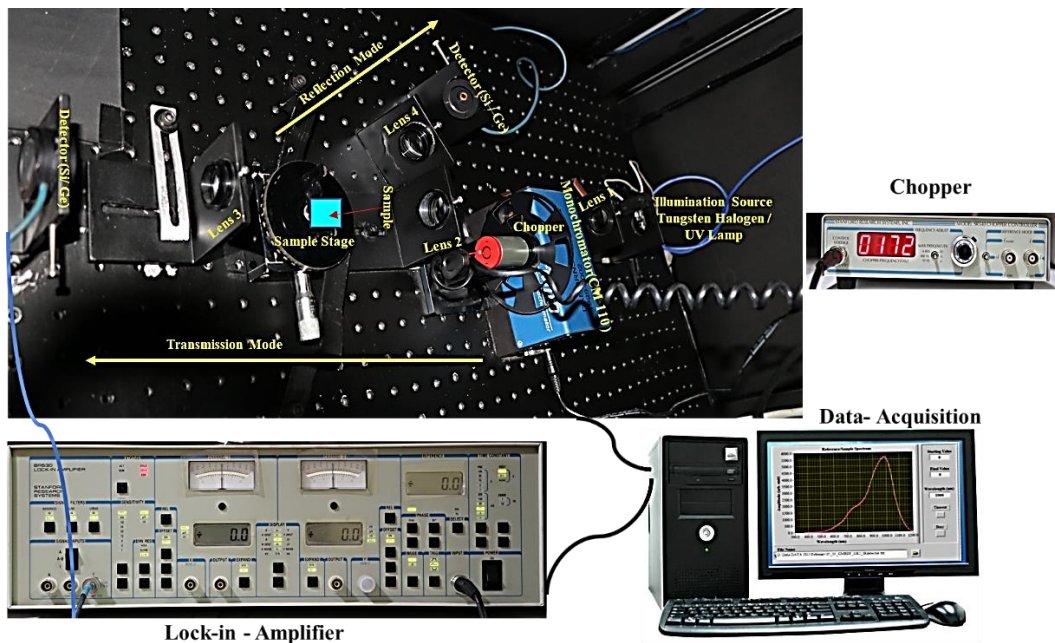


**Fig. 2.13: Optical -setup for UV-Vis-Near Infrared Spectroscopy.**

- [3] C. Suryanarayana and M. Grant Norton, *X-Ray Diffraction-A Practical Approach*, Springer, Boston, MA (1998).
- [4] Weilie Zhou, Robert P. Apkarian, Zhong Lin Wang and David Joy, *Fundamentals of Scanning Electron Microscopy*, Springer, New York (2006)
- [5] Ludwig Reimer, *Scanning Electron Microscopy- Physics of Image Formation and Microanalysis*, Springer, Newyork (1998).
- [6] Daisuke Shindo and T. Oikawa, *Analytical Electron Microscopy for Materials Science*, Springer, Japan (2002).
- [7] *What is X-ray Fluorescence Spectroscopy (XRF)* - HORIBA
- [8] Bert Voigtländer, *Scanning Probe Microscopy- Atomic Force Microscopy and Scanning Tunneling Microscopy*, Springer, New York (2015).
- [9] Sidney Perkowitz, *Optical Characterization of Semiconductors: Infrared, Raman, and Photoluminescence Spectroscopy*, Academic Press, San Diego, (1993).
- [10] Takeshi Aoki, *Characterization of Materials*, John Wiley & Sons, Inc (2012).

- [11] J. Van der Pauw, *Philips Research Reports*, **13** (1958) 1-9.
- [12] K. A. Emery, *Solar Cells*, **18** (1986) 251-260.
- [13] J. S. Hartman and M. A. Lind, *Solar Cells*, **7** (1983) 147-157.
- [14] Mark Fox, *Optical Properties of Solids*, Oxford University Press, New York (2001).